Limit Cycle Oscillating Detonation Wave Behavior Analysis within a Rotating Detonation Engine

Kristyn B. Johnson May[*], Justin Weber[†], and Don Ferguson[‡]
National Energy Technology Laboratory - U.S. Department of Energy, Morgantown, WV, 26505

Andrew Nix[§]
West Virginia University, Mechanical and Aerospace Engineering, Morgantown, WV, 26505

Todd G. Sidwell[**]
National Energy Technology Laboratory - U.S. Department of Energy, Morgantown, WV, 26505

Limit cycle oscillation (LCO) detonation wave behaviors are presented and analyzed for test times exceeding twenty seconds in a water-cooled rotating detonation engine (RDE). LCO detonation waves exhibit cyclic acceleration and deceleration, resulting in oscillating wave spacing at unique process conditions. In previous RDE studies, similar behaviors have been studied as microsecond scale instabilities leading to ascending or descending modal transitions. In the current work, however, LCO waves are considered a persistent wave mode, occupying unique portions of the operational envelope adjacent to those of their equally spaced counterparts. These occurrences of LCO waves are repeatable, enduring behaviors. A method to generate shifted contour surfaces specifically intended to extract and analyze wave spacing variation through time, termed limit cycle oscillation visualization (LCOV) surfaces, is presented. LCOV surfaces transform data into the reference frame of a primary traveling wave, are used to analyze quasi-steady, short timescale, and transitional LCO modes. Results are leveraged to understand the relationship between fill height, wave strength, local wave acceleration, and subsequent LCO wave spacing for individual wave sets. Quasi-steady LCO waves display wave spacing oscillations between equal spacing values associated with ±1 wave across runs exceeding 18 and 13 seconds, respectively.

Presented as Paper 2023-0931 at AIAA SciTech, National Harbor MD, January 23–27, 2023

[*] Research Engineer, Thermal Sciences, and AIAA Member. kristyn.johnson@netl.doe.gov
[†] Research Engineer, Thermal Sciences, and AIAA Member. justin.weber@netl.doe.gov
[‡] Senior Research Engineer, Thermal Sciences, and AIAA Member. donald.ferguson@netl.doe.gov
[§] Associate Professor, Mechanical and Aerospace Engineering, and AIAA Associate Fellow. andrew.nix@mail.wvu.edu
[**] Research Engineer, Thermal Sciences, and AIAA Member. todd.sidwell@netl.doe.gov

Nomenclature

A_c	=	carrier signal amplitude
f	=	frequency
f_c	=	carrier signal frequency
f_m	=	modulated signal frequency
f_Δ	=	peak deviation
l_{cr}	=	critical injection length
LCO	=	limit cycle oscillation
LCOV	=	limit cycle oscillation visualization
$\dot{m}$	=	mass flow rate
n	=	image index
p	=	smoothing parameter
P_{back}	=	backpressure
r	=	radius (pixels)
S_W	=	smoothing spline function for wave W
t_{mf}	=	fuel and oxidizer critical injection time
t_r	=	wave revolution time
$\overline{U_w}$	=	average wave speed (m/s)
U_{cj}	=	Chapman–Jouguet wave speed (m/s)
W	=	wave count/wave number
x_i	=	local maximum pixel intensity x-location
y_i	=	local maximum pixel intensity y-location
$y(t)$	=	frequency modulated signal
$\Delta\beta_{A-B}$	=	local LCO rate for generic wave set A-B
Δt_w	=	time differential between two waves
θ	=	angular/azimuthal location
Θ	=	detonation surfacfe matrix

Ψ	=	shifted LCO matrix
ρ_{pol}	=	polar image stack
τ	=	cumulative lag
ϕ_Z	=	integrated pixel intensity for azimuthal bin Z
Φ	=	equivalence ratio
ξ_W	=	wave intensity trace of wave W

I. Introduction

The United States Department of Energy, other government agencies, and private companies are investing in the development of rotation detonation engines (RDEs) for a variety of applications including gas turbines, rocket engines and aircraft propulsion due to the promise of increased efficiencies. Specifically for gas turbines, RDEs capable of producing a pressure gain across the combustor would provide a significant gain in cycle efficiency [1]. Additionally, promising low NOx emissions without pre-mixed air and fuel have been measured, allowing for stable hydrogen combustion without flash-back [2].

RDEs, rotating detonation combustors (RDCs), or rotating detonation rocket engines (RDREs) are generally described as combustors operating on gaseous, liquid, or even solid fuels that are specifically designed to sustain the circumferential propagation of one or more detonation waves in a confined annular or hollow cylindrical combustor. It is the promotion of the detonation waves, opposed to the suppression of combustion instabilities in typical combustors, which was proposed in the 1950s to 1960s as a method that could lead to higher performing rocket engines [3, 4]. Gas turbine engines offer an alternative application where the RDE is coupled to upstream and downstream turbomachinery as illustrated in Figure 1.

Modern gas turbine engines incorporate highly efficient (>90%) compressors and turbines that are designed to function in steady flow with an optimized pattern factor. However, exhaust flow from an RDE is unsteady leading to spatiotemporal variations in pressure, temperature, and velocity. Unless the turbine can effectively ingest the unsteady flow, a pressure gain from the RDE may not translate to an increase cycle efficiency. Therefore, it is imperative that detonation wave dynamics are well characterized so that future transition elements and turbine designs can efficiently convert the energy in the fluid to work.

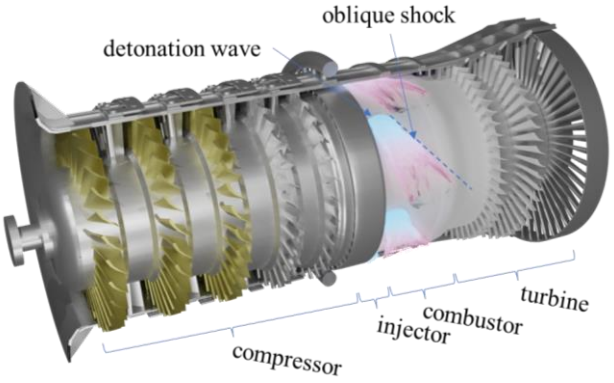

Fig. 1 Artistic interpretation of a hypothetical gas turbine rotating detonation engine.

The focus of this study is on the stability of the detonation wave within the combustor with particular emphasis to the analysis of *limit cycle oscillation* (LCO) waves, where the wave speed and subsequent wave spacing (for multiple wave modes) exhibit periodic, and non-periodic variations. Among the behaviors observed, a varying degree of wave separation and cyclic behaviors contribute to multiple types of LCO behavior: quasi-steady, short timescale, and transitional. The detection of each type may offer vital information regarding the causes and implications of each category.

Variations in detonation wave stability have been observed in rotating detonation engines in multiple studies [5, 6], and is often observed as unsteady or transitional behavior between wave modes or leading to wave failure. Bennewitz et al. witnessed a brief unsteady oscillating behavior during transition from two to three waves and again from three to two waves, across 1.76 and 3.08 msec, respectively, corresponding to changes in the reactant flow rates [5]. Alternatively, Koch et al. characterized oscillating wave behavior observed in their short-duration experimental RDE as a natural dynamic state which does not necessarily lead to wave failure [7]. Instead, it is the result of non-linear interactions of multiple time scale unit processes, including injection and mixing, combustion, exhaust, and wave propagation, which lead to a global dynamic state. The time scales of these states are dictated by the boundary conditions of the RDE and can be adjusted by changing the process conditions such as the equivalence ratio, flow rates, and back pressure.

Similarly, Wolański proposed a simple detonation wave model relating two-unit process time scales, namely the injection of the fuel and oxidizer and the wave propagation [8]:

$$W = 2\dot{V}_t / h l_{cr} U_w \tag{1}$$

where W is the wave count, $\dot{V}_t$ is the Total volumetric flow of reactants, h is the width of the combustor annulus, l_{cr} is

a critical length of the reaction zone often related to detonation cell size, and U_w is the detonation wave speed. Wolański suggested that W of less than one would result in unstable detonation ultimately leading to wave failure establishing a form "*galloping rotational detonation*" behavior. The author noted that while there were similarities in behaviors such as wave acceleration, deceleration and intermittent failures, the mechanisms associated with "*galloping rotational detonation*" differed from classical galloping detonation. And while the relationship expressed in Equation 1 attempts to provide some measure of detonation wave stability for a single wave, criteria for multi wave stability such as wave speed non-uniformity and modal transitions has not been established. This would require the addition of other dynamic time scales as suggest by Koch et al. [7].

Combustion instabilities observed in previous RDE literature [5, 6, 8], as well as other classic detonation studies, may differ from those discussed here in that previous observations were made over very brief periods of time (i.e., single shot detonation or durations of less than a few seconds in RDEs). The *limit cycle oscillations* discussed in this work are observed over periods many orders of magnitude longer, resulting in example cases that include stable global dynamics where LCO modes persist, as well as global dynamic transitions from uniformly spaced detonation waves to quasi-steady LCO modes. Many runs containing similar transitions and/or immediate establishment of quasi-steady LCO waves have been observed throughout extended runs exceeding 20 seconds. Therefore, consideration of LCO waves as a repeatable, persistent, and preferred wave mode of operation, instead of uniformly spaced waves, at certain process conditions is needed. Shifted detonation surfaces, generated from high-speed images, facilitate the measurement of angular separation between neighboring waves through time revealing LCO as well as steady behaviors. The method to create the shifted contours is briefly presented in Section V.

II. Experimental Facility

A graphic representation of the water-cooled RDE test rig used in this study is given in Figure 2. The water-cooled RDE is constructed of 315 stainless steel with the ability to operate up to 20 bar for extended test times, although run times are typically limited to no more than 30 seconds which is adequate to achieve a thermally steady state while conserving fuel. The RDE used in this study is configured with axial air and acute angle fuel injection resulting in an air inlet minimum area ($A_{3.1}$) or 1262mm^2. The combustion channel has an inner and outer diameter of 128.5mm and 148.8mm, respectively, resulting in a ratio of channel area to injector area ($A_{3.2}/A_{3.1}$) of 3.5. An exit nozzle with a minimum area of 3371mm^2 ($A_8/A_{3.2}$ = 0.76) is located at the end of the 76.2mm long combustion channel.

Immediately downstream of the exit nozzle is an exhaust diffuser used to slow the supersonic exit flow of the RDE to subsonic speeds consistent with the design of conventional stator or turbine inlet vanes. Immediately downstream of the diffuser, the exhaust duct reaches a diameter of 154 mm and is tied with the exhaust flow turning 90° where it flows through a high-pressure backpressure valve and ultimately vents to atmosphere. At the tee, a 101.6mm fused silica window with nitrogen purge is positioned to provide down-axis images of combustion occurring in the RDE. Elements of the test article are water-cooled until 1.5m downstream of the exhaust tee that ties to the imaging port where the remaining exhaust duct is refractory lined until it is vented to atmosphere.

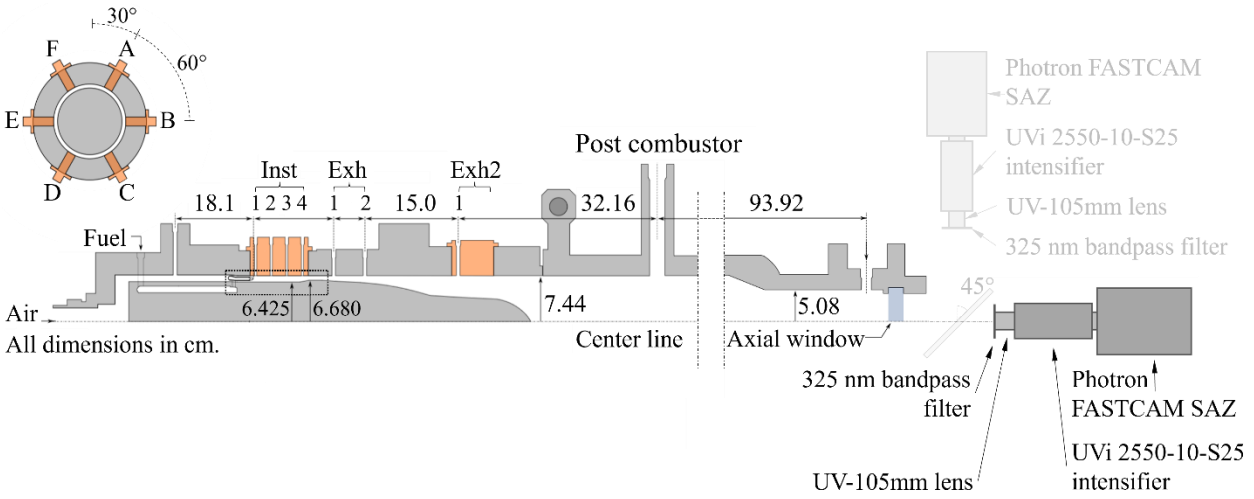

Fig. 2 Cross-section water-cooled RDE showing axial injection, port nomenclature, exit nozzle, diffuser, and high-speed imaging setup. Box indicates Figure 3 boundary.

A methane-air flame located just downstream of the diffuser in the exhaust duct provides both fuel scavenging and primary ignition for the RDE. A typical test sequence begins with combustion air set at the desired mass flow rate, inlet temperature and exhaust pressure. The main fuel (hydrogen) valve is opened at the desired mass flow rate with ignition occurring at the post-combustor and propagating upstream to the injector dump plane, transitioning from deflagration to detonation.

Figure 3 shows a detailed view of the detonation channel, which is outlined in Figure 2, with station numbers according to Brohpy et al. [9]. The *pintle* injector splits the air flow into inner and outer rings, with the fuel entering the center of the injector. The fuel is used to cool the tip of the injector before exiting through 240 0.76-mm diameter holes to mix with the air at the start of the detonation channel. Six water-cooled instrumentation modules are equally spaced circumferentially around the detonation channel with each module having four axial ports that access the

combustion channel and are separated by 25.4mm with the first port located 2.5mm from the end of the injector. The sample positions are identified by the module circumferential location, labeled A-F clockwise looking downstream, and the axial location, assigned port numbers 1-4 increasing in value downstream of the injector exit. For example, a transducer located in module E position 1 would be designated as E1. This port would be physically located 270° circumferentially and 2.5mm axially from the end of the injector geometry.

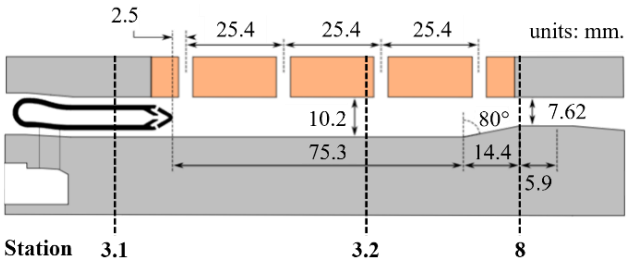

Fig. 3 Axial air injection, combustion channel and exit nozzle with air injector throat (3.1), combustion channel gap (3.2), and exit nozzle throat (8) station designations.

A variety of measurement techniques are employed in the sampling ports including capillary tube averaged pressure (CTAP), infinite tube pressure (ITP), ion probes, fiber based OH* chemiluminescence and thermocouples. The CTAPs consist of a 2 m long, 0.794-mm diameter capillary with an Omega PX309-100G5V pressure transducer at the end. The ITPs consist of a 4.57-mm diameter tube with a PCB model CA102B06 installed in a tee perpendicular to the flow approximately 152mm from the combustion channel, followed by 6 m of tubing with a cap on the end. Ion probes (+15V) are constructed of a 1.5mm tungsten rod surrounded by a ceramic tube to keep it electrically isolated from the RDE walls which provide electrical ground. The final instrument typically used is a OH* chemiluminescence probe, which consists of a 1mm N_2-cooled fused-silica fiber optic recessed 2mm from the 3.88mm diameter port to the combustion channel. This provides a view of approximately 17° along the inner diameter of the RDE. The fiber is coupled to a UV bandpass filtered centered at 325nm (FWHM = 110nm) leading to a Hamamatsu R212 photo-multiplier tube (185 to 650 nm spectral response, maximum response at 340 nm).

Process control including air and fuel flow rates, exhaust back-pressure and combustion air inlet temperature are controlled by an Allen-Bradley process control system, while primary data acquisition is managed by multiple National Instruments I/O modules (PXIe-6366 and PXIe-6338) with a PXIe-8880 Xeon Controller running LabVIEW software. Sampling rates range from 1 Hz through 1 MHz depending on data type and measurement technique.

III. Image Treatment

The RDE has optical access through an axial window placed approximately 1.5 m from the RDE exit plane, past the exhaust tee, Figure 2. Imaging of the RDE annulus is performed with a Photron FASTCAM SAZ camera at 60,000 fps (frames per second) in conjunction with an Invisible Vision UVi 2550-10-S25 intensifier, Nikkor UV-105mm UV lens, and UG11 325 nm bandpass filter (FWHM = of 110 nm). The intensifier provided a gate width of 14 μsec to limit travel of the detonation wave (~28mm at a wave speed of 2000 m/sec, or 6.5% of the mean annulus circumference) within a single image. In previous literature utilizing OH* chemiluminescence images captured at the NETL RDE facility, imaging hardware has been positioned at a 90° offset in relation to the RDE axis, shown opaquely in Figure 2. This method is widely used to protect the imaging equipment at risk of damage if the axial window were to fail. The majority of images utilized in this study are captured with the imaging system positioned along the centerline of the combustor (Figure 2) as this is found to improve image quality. Images are captured with dimensions 512 x 512 pixels, offering a resolution of approximately 0.397 mm/pixel.

To acquire images throughout the 20 to 30 second test run given limited on-board camera memory, a 5V square wave with a frequency of 2 Hz and a duty cycle of 3.5% is used to trigger the camera. Coupled with a frame rate of 60k fps, this results in 1050 images acquired every 0.5 sec throughout the test run. From these, 1024 continuous images are used to determine the wave mode and speed by calculating a 2D Fast Fourier Transform (FFT) of the detonation surface [10].

IV. Method

To analyze both short and long timescale LCO behaviors, a method to transform the well-established and widely used detonation surface [10, 11] to a traveling wave reference frame, referred to in this paper as *limit cycle oscillation visualization* (LCOV), is used to extract the local angular spacing between individual waves. permitting the characterization of the wave dynamics and correlation to other variables. Transforming data into the reference frame of a primary wave is similar to the work of Koch [7] who transformed detonation surfaces into the mean-velocity reference frame as well as other phase reduction techniques applied to a variety of scientific and experimental data. In this instance, it is uniquely employed to investigate varying timescales of LCO behavior in RDEs which have otherwise been viewed only as microsecond scale instabilities.

To extract the detonation wave surface, the detonation channel is identified spatially in the filtered image stack containing N images. Next, a polar mesh centered about the annulus is used to partition the polar image stack, ρ_{pol}, into equally spaced azimuthal bins along the RDE channel. Plots presented throughout the text are generated using 360 polar bins, each spanning 1.0°, and an RDE gap width of 24 pixels, stated in Equation 2. For a given image, n, an integrated pixel intensity is determined for each bin, ϕ_z, according to Equation 3. Because $\Delta\theta$ equals 1.0°, θ_2 and θ_1 correspond to values of z and $(z-1)$, respectively. Finally, a series of images are processed, integrated intensities of each bin are then concatenated into a detonation surface matrix, $\Theta(z, n)$, according to Equation 4 [10]. These steps form a 2D array depicting angle and time, where each row (z) represents a radial location from the first to the Z^{th} bin and each column (n) represents an image frame up to the N^{th} frame in the time interval of interest. An example detonation surface used to illustrate the image processing method is shown in Figure 4 (top), where the visible linear traces depict a detonation wave passing through time and angular locations. In this format, slope magnitudes of the visible wave traces correspond to the angular velocity of individual waves, and the sign of the slope to wave direction. Specifically, positively sloped traces indicate counterclockwise waves, while negatively sloped traces indicate clockwise waves.

$$\Delta\theta = 1.0^\circ \quad \Delta r = 24 \text{ pixels} \tag{2}$$

$$\phi_z(n) = \int_{r_1}^{r_2} \int_{\theta_1}^{\theta_2} \rho_{pol}(r, \theta, n)\, \mathrm{d}\theta dr \tag{3}$$

$$\Theta(z, n) = \begin{bmatrix} \phi_{1_1} & \phi_{1_2} & \phi_{1_3} & \cdots & \phi_{1_N} \\ \phi_{2_1} & \phi_{2_2} & \phi_{2_3} & \cdots & \phi_{2_N} \\ \vdots & \vdots & \vdots & \ddots & \vdots \\ \phi_{Z_1} & \phi_{Z_2} & \phi_{Z_3} & \cdots & \phi_{Z_N} \end{bmatrix} \tag{4}$$

The proposed method shifts each column of the detonation surface matrix in a manner such that a primary (reference) wave is held at a single angular location, which is akin to shifting from a laboratory to a detonation wave frame of reference albeit to a single "primary" wave (W1). The selection of a primary (reference) wave is arbitrary as the waves are not defined as having unique properties when compared to other waves. Assigning a wave as "primary" provides a means of documenting relative behaviors between waves. It is not in reference to observed unique behaviors. The cumulative lag, $\tau(n)$, corresponding to each frame, n, provides a measure of the relative wave speeds, and is determined via Equation 5, where ★ denotes the cross-correlation of two signals, namely the integrated pixel intensities found by Equation 3. The cross-correlation is computed for two subsequent columns of the $\Theta(z, n)$ matrix,

being $\Theta(:, i)$ and $\Theta(:, i-1)$. At each iteration, the local lag of the n^{th} and $(n-1)$ columns corresponds to the frame-to-frame angular progression of the primary wave. The first frame or column remains un-shifted, requiring the cumulative lag to be computed for columns 2 through n.

To begin constructing the shifted LCOV surface, $\Psi(z, n)$, the first column is directly transferred from that of $\Theta(z, 1)$. Thereafter, each column is constructed by circularly shifting the corresponding columns of $\Theta(z, n)$ by the cumulative lag, $\tau(n)$. According to Equation 6, column $\Psi(:, n)$ becomes $[\phi_{[1-\tau(n)]n}, \phi_{[2-\tau(n)]n}, \cdots, \phi_{[Z-\tau(n)]n}]$. An example shifted detonation surface, derived from Figure 4 (top), is shown in Figure 4 (center).

$$\tau(\mathrm{n}) = \sum_{\mathrm{i}=1}^{\mathrm{n}} [\Theta(:, \mathrm{i}) \star \Theta(:, \mathrm{i}-1)] \quad \in \quad [2{:}\,\mathrm{n}] \tag{5}$$

$$\Psi(z, n) = \begin{bmatrix} \phi_{1_1} & \phi_{[1-\tau(2)]_2} & \phi_{[1-\tau(3)]_3} & \cdots & \phi_{[1-\tau(N)]_N} \\ \phi_{2_1} & \phi_{[2-\tau(2)]_2} & \phi_{[2-\tau(3)]_3} & \cdots & \phi_{[2-\tau(N)]_N} \\ \vdots & \vdots & \vdots & \ddots & \vdots \\ \phi_{Z_1} & \phi_{[Z-\tau(2)]_2} & \phi_{[Z-\tau(3)]_3} & \cdots & \phi_{[Z-\tau(N)]_N} \end{bmatrix} \tag{6}$$

To illustrate the circular column shifting performed by Equations 5 and 6, integrated pixel intensities are plotted against angular location for three un-shifted frames in Figure 5 (top). For the simple two-wave case, each wave visibly propagates forward in angular location in each frame. Maintaining the azimuthal location of the primary wave, denoted W1, as it is found in the first frame, the cumulative lag is computed for the second and third frame. The shift of two detonation surface columns following the establishment of the primary wave location is illustrated in Figure 5 (bottom). It is shown that in the initial arrangement in Figure 5 (top), both waves propagate forward. In the shifted arrangement in Figure 5 (bottom), the location of the primary wave is standardized, allowing the spacing between W1 and W2 to be visualized and measured independent of average frequency. This transformation changes the detonation surface from the laboratory reference frame to the primary wave's reference frame. Throughout the manuscript, LCOVs are generated for sample windows of 200 frames, approximately 3.33 msec.

The same shifting method can also be applied for detonation surfaces with larger wave quantities, such as the four and five wave cases described in the next section. There again, the locations of each wave initially propagate through successive frames. After the shifting is executed for each column, W1 is aligned throughout the sample window and wave-to-wave angular spacing can be measured through time.

Following the construction of the shifted detonation surface, $\Psi(z, n)$, wave traces can be detected and described by a spline function. A smoothing spline, $\mathcal{S}$, can be constructed for each wave trace contained in the shifted detonation

surface, where x_i and y_i data correspond to local maximum integrated pixel intensity coordinates. Local maximum data representing a given wave in the primary wave's reference frame is used to fit a smoothing spline which minimizes Equation 7, where p is the smoothing parameter, typically set to 0.15. On occasion, the cumulative lag underestimates the necessary shifting values. To account for this, and to further standardize the LCOV plots, a spline is first fit to the primary wave, plotted as a red line in Figure 4 (center). Any deviation from the standard location is used to fine-tune the shift of each column so that the primary wave rests along a single angular index. The finalized LCOV contour is plotted in Figure 4 (bottom) with individual wave splines overlaid as red traces in Figure 4 (center).

$$p\sum_i \left(y_i - S(x_i)\right)^2 + (1-p)\int \left(\frac{d^2S}{dx^2}\right)^2 dx \tag{7}$$

Using the spline fit of individual wave traces enables further analysis of wave spacing, LCO acceleration, pixel intensity variation, and other parameters explored in the following section. Additionally, the piece-wise splines can be leveraged to visualize wave progression and spacing through a series of images. To visualize and confirm the limit cycle nature of this wave mode, the relationship between wave-to-wave pixel variation and angular spacing can be extracted through a series of frames. A clear limit cycle structure is observed in Figure 4 (bottom) using data extracted from the LCOV contour and splines associated with W1 and W2 in Figure 4 (center).

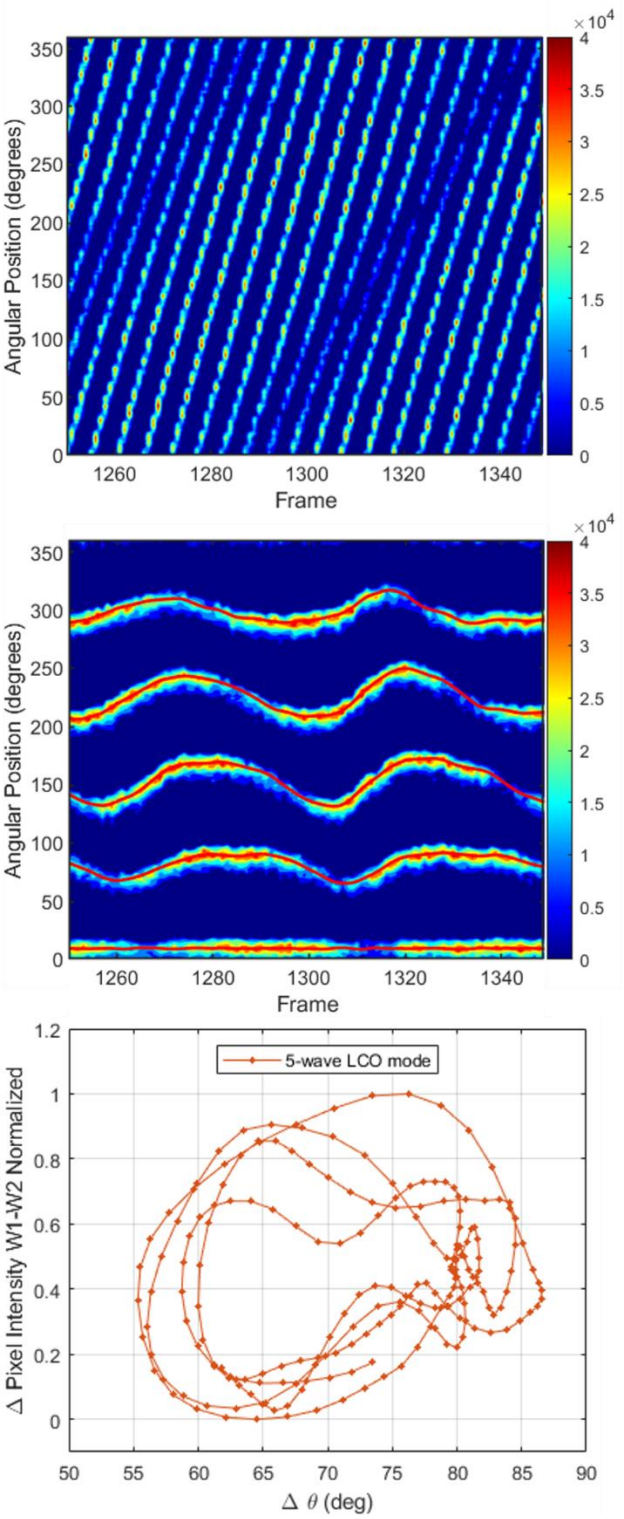

Fig. 4 Detonation surface (top), finalized LCOV (center), and limit cycle relationship for wave pair (bottom).

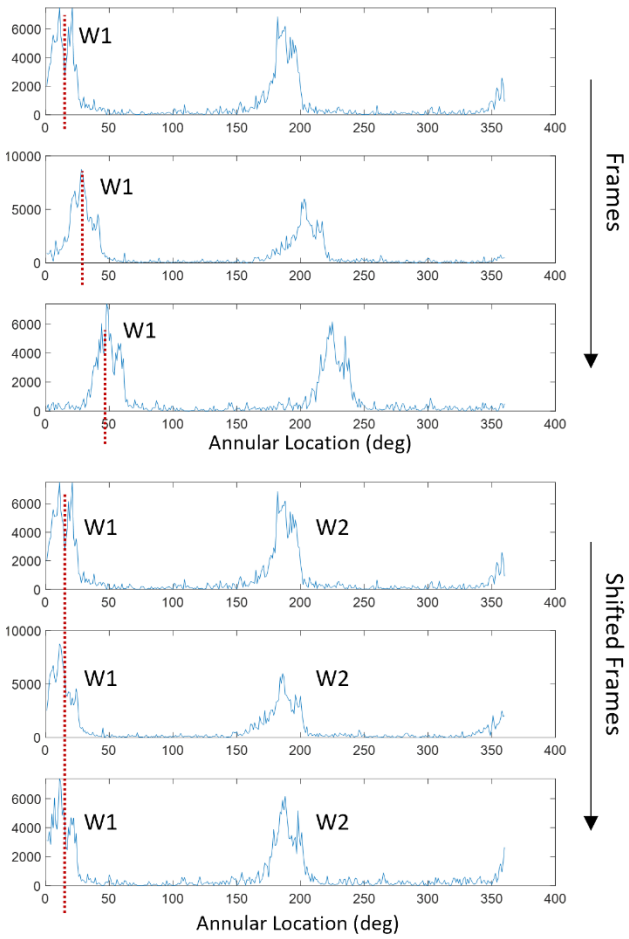

Fig. 5 Traces along azimuthal direction at two successive frames within a 2-wave detonation surface, shifted to align primary wave.

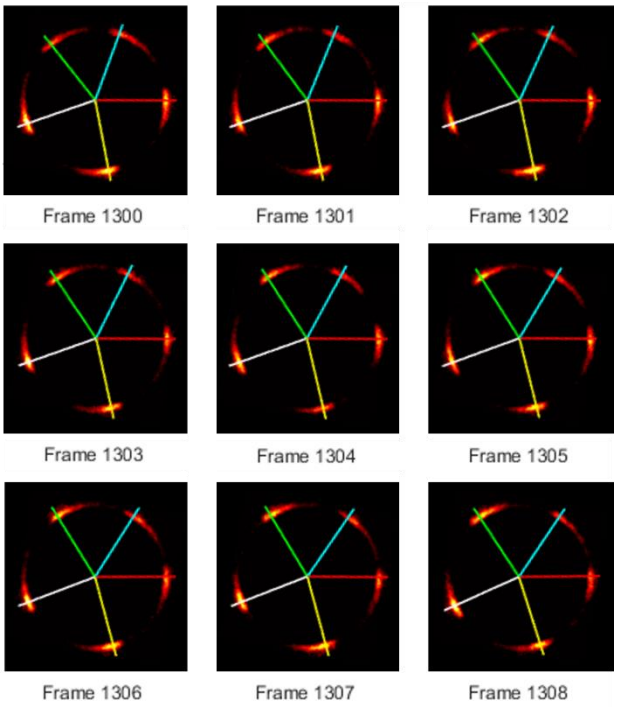

Fig. 6 Rotated high-speed OH* images to create stationary primary wave, with individual wave locations overlaid, sub-sampled from Figure 4.

Figure 6 shows a subset of raw, high-speed OH* chemiluminescence images used to generate Figure 4. Frames in Figure 6 are uniquely rotated about the center pixel at angles equal to their cumulative lag. This provides a shift from the laboratory to detonation wave frame of reference and maintains a constant primary wave position, indicated by the red polar line. Splines are used to overlay polar lines for additional waves, which illustrates wave spacing variation from frame to frame. In the subplot of Figure 6, Frame 1300 shows waves somewhat equally spaced around the expected 72° five-wave spacing. In just nine frames, 150 μsec, individual spacings fluctuate until Frame 1308 experiences a decrease in spacing between waves one and two (red and cyan lines), much closer to an equal six-wave spacing, and broader spacing between waves three, four and five (green, white and yellow lines), similar to that expected of equal four-wave spacing. This repeatable periodic behavior of LCO wave distance is investigated across a variety of operating conditions and observed LCO wave quantities in the following section.

V. Results

LCO waves observed with the NETL RDE are repeatable and constitute a stable (persistent) mode dependent on the operating conditions. The results presented here are selected to best represent the three types of wave-spacing

oscillations that are typically seen: quasi-steady oscillations (Q), short timescale oscillations (S) and oscillations occurring through operational transitions (T). For each classification, multiple data points are presented with varying wave counts. Table 1 summarizes the LCO cases according to type, wave count, case descriptor, equivalence ratio, Φ, mass flow rate, $\dot{m}$, backpressure, P_{back} (psig), and imaging alignment. Case descriptors (detailed above) will be used throughout the text with a nomenclature structure of a type descriptor followed by wave count. Transitional case descriptors (T) are unique in that wave counts incrementally change due to actively changing equivalence ratios. Therefore, transitional wave counts include two-digit descriptors indicating initial and final wave counts.

Table 1 Summary of LCO cases presented in the following subsections.

Type	Wave Count	Case Descriptor	Φ	$\dot{m}$ [kg/sec]	P_{back} [kPa]	$\frac{\overline{U_w}}{U_{cj}}$[%]	Imaging Setup
Quasi-steady	4	Q4	0.5	0.61	0	61	Perpendicular
	5	Q5	0.72 → 0.55	0.95	0	58 → 61	Center-aligned
Short Timescale	2	S2	0.93	0.71	0	72	Perpendicular
	4	S4	0.64	0.61	0	59	Perpendicular
Transitional	4-5	T45	1.0 → 0.48	0.95	69	66 → 57	Center-aligned
	5-4	T54	0.49 → 0.90	0.95	69	59 → 67	Center-aligned

A. Indications of LCO Modes

Evidence of LCO wave modes is also present in other high-speed point measurements such as pressures, ion probes, and OH* chemiluminescence (~17° view of inner diameter). LCO waves can be identified by the presence of sidebands accompanying the peak carrier frequency in the spectrogram. These same side bands can also be seen in the spectrograms of the ITPs and ion probes. One interesting variation of LCO mode presentation is observed in short timescale LCO cases, where limit cycle behavior is present but smaller scale modulations do not present strong sidebands in the spectrogram. These less drastic LCO conditions may be overlooked due to weaker sidebands and must further be detected and confirmed using the LCOV method, and will be expounded upon in a later subsection. An example of typical LCO behavior is observed in the 1MHz sampled normalized OH* signal shown in Figure 7. Conversely, Figure 8 shows a wave-count normalized OH* probe signal and an extracted FFT from the spectrogram of a non-LCO mode in which there are no sidebands present. Other researchers have also seen these sidebands in spectrograms [12, 13, 14]. In the example of Figure 7, it is the consistent modulating frequency (f_m) of the changes in wave spacing that cause the sidebands to be visible in the spectrogram. This frequency modulation can be extracted by determining the spacing of the peaks as shown in Figure 7(b). In this example, the dominate carrier frequency (f_c)

of 9.1 kHz is measured, with a modulation frequency (f_m) of 1.4 kHz, indicating an LCO behavior of the detonation waves. As discussed later, it is believed that periodic acceleration and deceleration of the waves result in the occurrence of the sidebands as opposed to bounded gradual and/or random changes in wave speed that would result in a broadening of the peak. Without high-speed imaging or highly spatially resolved point measurements, it is difficult to confirm LCO behavior solely based on observation of periodic changes in the peak height because other behaviors, such as counter rotating waves, can also generate similar time series traces [15, 16].

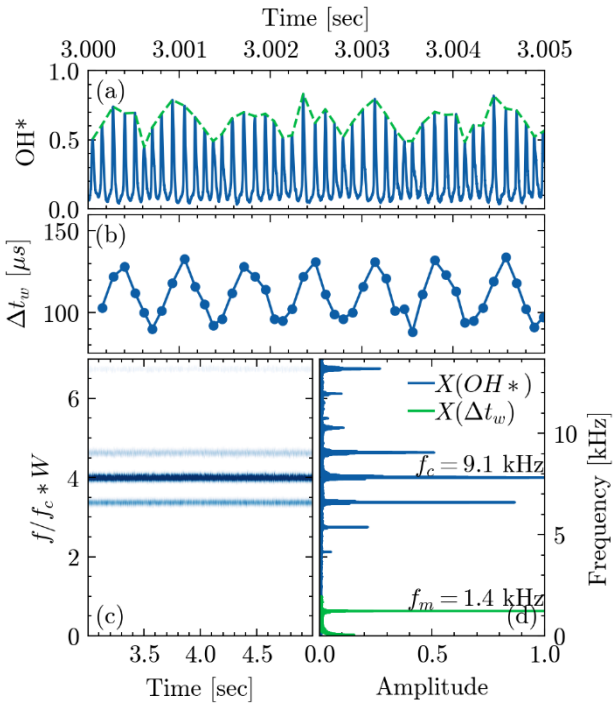

Fig. 7 OH* data (a); peak spacing (Δt_w) (b); OH* spectrogram normalized to wave count (c); OH* and wave spacing FFTs (d) for four-wave LCO condition (Q4).

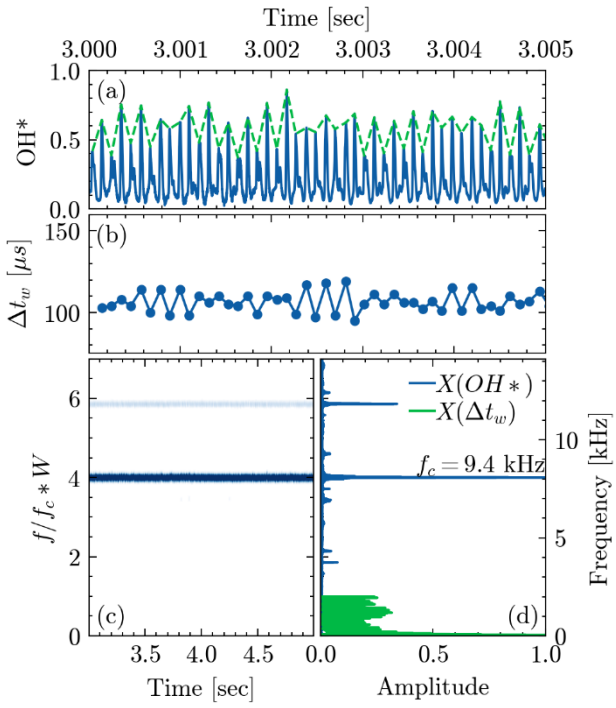

Fig. 8 OH* data (a); peak spacing (Δt_w) (b); OH* spectrogram normalized to wave count (c); OH* and wave spacing FFTs (d) for four-wave non-LCO condition (S4).

B. Quasi-steady LCO Waves

Others have characterized wave spacing oscillations occurring with rotating detonation as modal instability [8]. In short timescales, rapid changes in wave spacing can result in the extinguishing of a weakened wave, or the addition of a new wave. In those cases, changes in wave spacing results in an ascending or descending modal change, which results in a classification of instability [5]. However, extended observation of this mode, tends to suggest repeatable and consistent LCO states.

For example, Figure 9(a) shows the spectrogram of the OH* probe and equivalence ratio for test case Q4. The combustor is operated at a target equivalence ratio of 0.5, mass flow rate of 0.61 kg/sec, atmospheric back pressure, and a combustion air inlet temperature of 477.6 K. After the initial start-up transient, the process reaches a steady state with a four-wave persistent LCO mode remaining persistent throughout the entire 20 second test run as indicated by the equally spaced main carrier frequency sidebands. A modulation frequency (f_m) of 1.4 kHz is consistent during the duration of the test. Based on the dominate frequency and the four-waves, a mean average wave speed is determined to be 61% of the CJ wave speed. Figure 9(b) shows the average wave speed normalized by CJ speed alongside the CJ speed throughout the entire run.

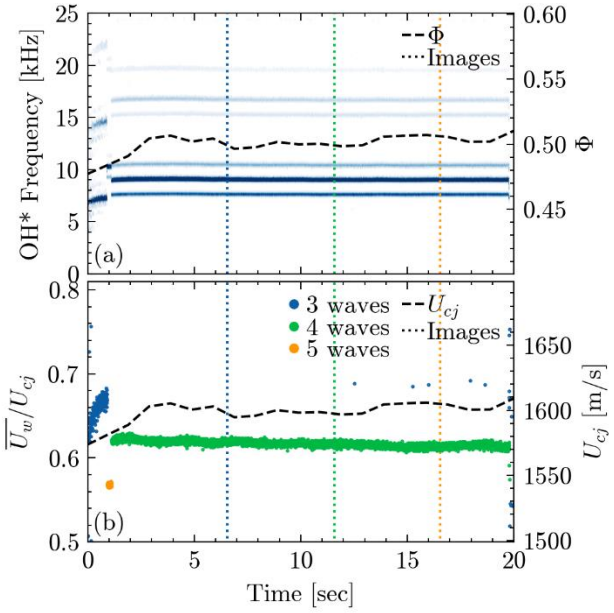

Fig. 9 OH* probe spectrogram for quasi-steady four-wave LCO (Q4) with equivalence ratio (a) and average wave speed normalized by CJ speed with the CJ speed (b).

Figure 10 shows the detonation surface, LCOV surface, and extracted wave separation for each of the three selected times overlaid as vertical dashes in Figure 9. The LCOV surface and wave separation plots clearly display the periodic instability of the wave spacing indicative of the limit cycle oscillations that persists across the multiple times shown across the three plots. In this format, it is seen that the wave spacing between the individual waves is modulating between a uniform three wave spacing (120°) and five wave spacing (72°). Wave spacing traces also suggest that the periodic behavior is not unique to a single wave set, (angular separation of neighboring waves) nor is any individual wave passive in interacting with either neighboring wave. This demonstrates that while there is a clearly dominant

frequency presented by the spectrogram in Figure 9, there is no dominant wave driving the LCO behavior. Instead, the period of each wave spacing trend is comparable, indicating a reciprocating exchange of local wave acceleration and available fill height. This concept will be further discussed in subsection VI.E.

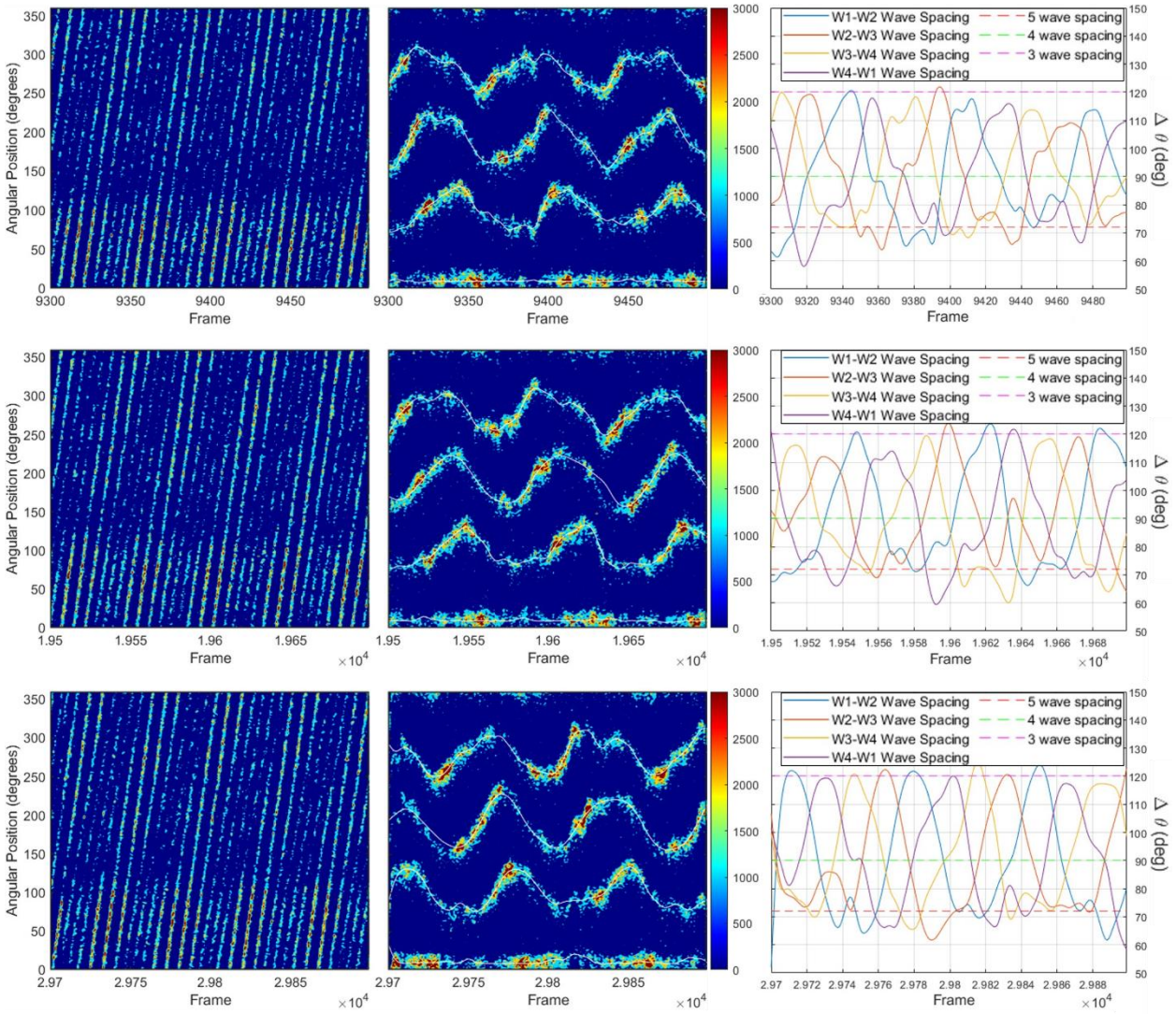

Fig. 10 Quasi-steady LCO detonation surface Q4 (left), LCOV surface (center), and wave separation (right)

Similar to case Q4, a five-wave LCO mode is observed via a spectrogram for the duration of test run Q5 aside from the initial start-up transient, shown in Figure 11(a). However, unlike previous tests the equivalence ratio is intentionally reduced linearly from 0.72 to 0.55 over the course of the approximately 14 second test, as depicted in Figure 11(a). Once the LCO behavior is established at the start of the test, it remains persistent without mode change, although there is a noticeable decrease in the mean wave speed which is consistent with the change in equivalence ratio. As the equivalence ratio decreases, the mean wave speed normalized by the CJ speed increases from 59% to

61%, shown in Figure 11(b). This further supports the notion that the LCO may be a stable mode of operation for the RDE. Sidebands at the three sampling points of 6.073, 11.073, and 13.573 seconds show a comparable drop in the sideband frequency to that of the primary wave mode, maintaining a constant modulation frequency (f_m) of 1.1 kHz, suggesting a persistent relationship between the primary wave mode and LCO behavior.

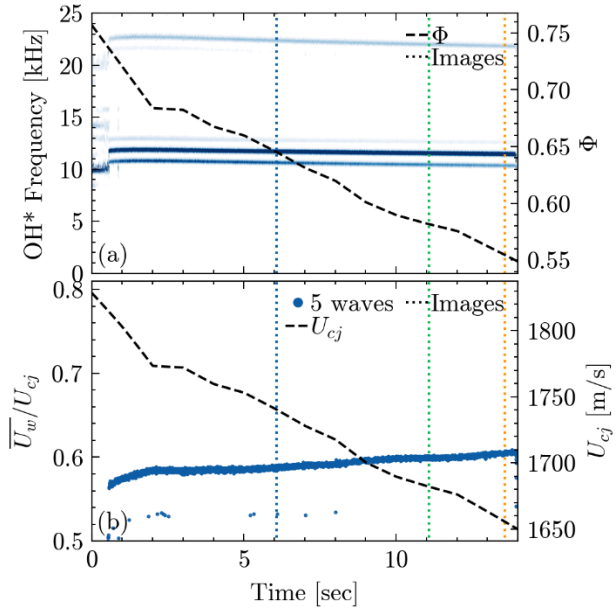

Fig. 11 OH* probe spectrogram for quasi-steady five-wave LCO (Q5) with equivalence ratio (a) and average wave speed normalized by CJ speed with the CJ speed (b).

The Q5 LCO wave mode is demonstrated in detonation surfaces and subsequent LCOV surfaces shown in Figure 12 (left) and (center), respectively. Periodic instances of lower chemiluminescence intensity can be observed in the detonation surfaces and LCOV surface plots, correlating with the wave spacing. This could suggest a periodic change in fill height potentially driven by the refresh rate of the fuel and/or air injection although evidence against it being a data acquisition artifact would need to be shown to be more conclusive.

Wave spacing for five equally spaced waves would be 72°. However, five wave LCO wave spacing plotted in Figure 12 (right) varies from 50° to 85°. From top to bottom in Figure 12, the equivalence ratio is decreasing. Interestingly, even with the stated decrease in equivalence occurring in Q5 and subsequent decrease in wave speed as observed by the primary wave frequency, the LCO wave spacing of 50° – 85° remains consistent over the entire test run.

Throughout the testing envelope, LCO cases are typically observed at intermediate equivalence ratios which are leaner than that required of an equally spaced mode of the same wave count, but richer than that required to establish

an additional detonation wave. This trend is intuitively related to the general wave spacing oscillations between equal spacing values associated with ±1 wave. A decreased equivalence ratio enables intermediate confined wave spacing up to a critical point just below what can be sustained by an equivalence ratio associated with an incrementally higher wave count. Associations of wave spacing acceleration and wave strength are discussed at greater length in subsection VI.E.

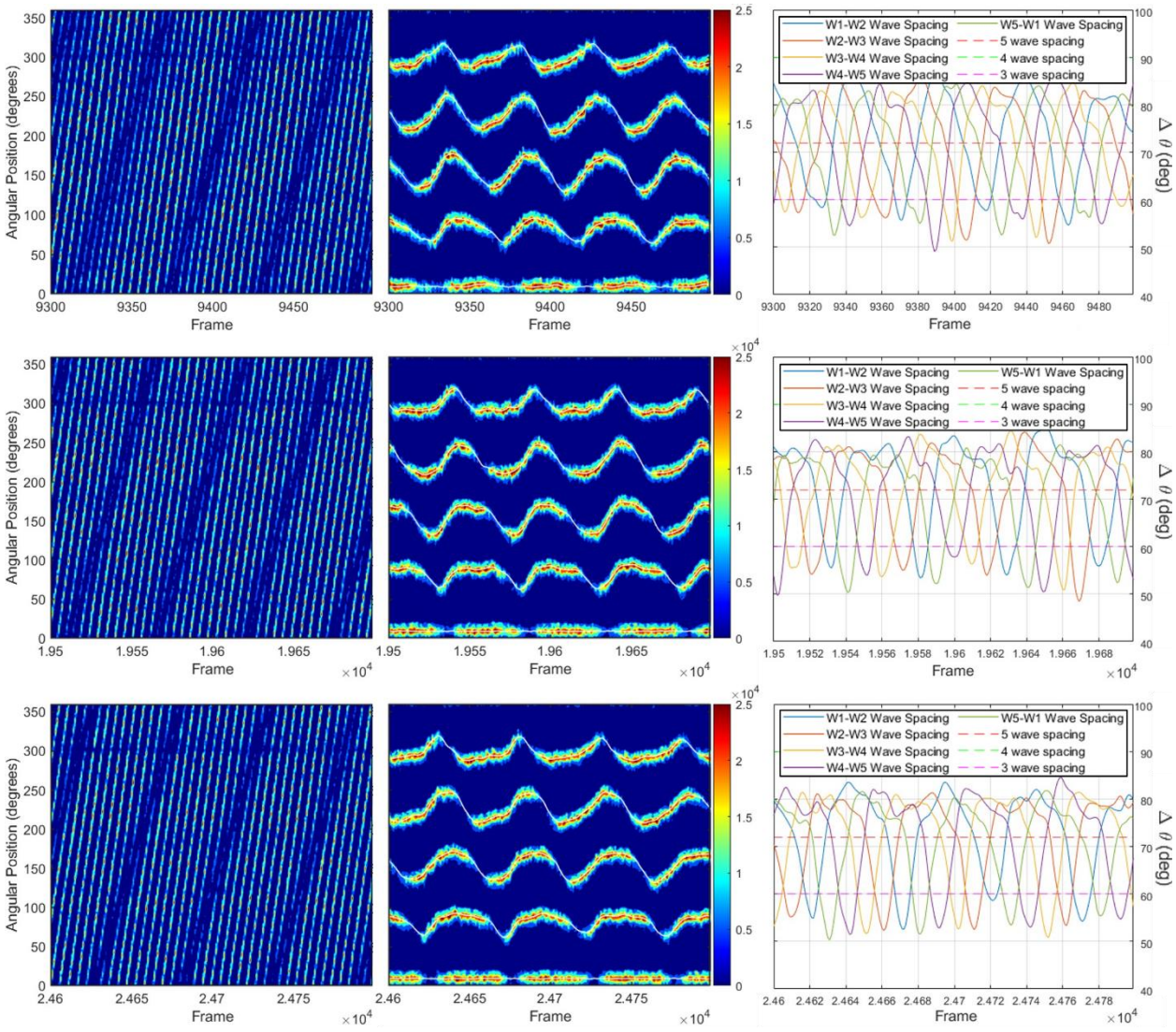

Fig. 12 Quasi-steady LCO detonation surface Q5 (left), LCOV surface (center), and wave separation (right).

C. Short Timescale Oscillations and Variations

Wave spacing variation has also been observed within short time and length scales, even when indicators extolled in Section VI.A of an LCO mode are not present. Case S2 consists of an operating mode composed of two co-rotational waves with the OH* spectrogram given in Figure 13(a). At a steady mean equivalence ratio of 0.93 during the test

duration, plotted in Figure 13(a), the mean wave speed is 72% of the CJ speed, depicted in Figure 13(b). Weak sidebands indicative of LCO are present in the spectrogram with a modulation frequency (f_m) of 2.3kHz. Additionally, small wave spacing oscillations can be seen in the LCOV shown in Figure 14 (center). By fitting splines to both the primary and secondary waves in Figure 14 (center), the angular separation can be calculated and plotted, as is shown in Figure 14 (bottom). In the case of S2, the wave separation oscillates around the persistent, two-wave spacing (180°) but is limited to oscillations falling within ±10°. For these reasons, short timescale oscillations in S2 are deemed LCO.

Table 1 provides the operational conditions resulting in case S4, which is made up of four equally spaced waves after the initial start-up transient as shown in Figure 15(a). The equivalence ratio is consistent, at a value of 0.64, during the 20 second test, recorded in Figure 15(a). The mean wave speed is 59% of the CJ speed, which is shown in Figure 15(b). The spectrogram is dominated with a single frequency band, and subsequent harmonics. Side bands on either side of the dominate frequency are not visible.

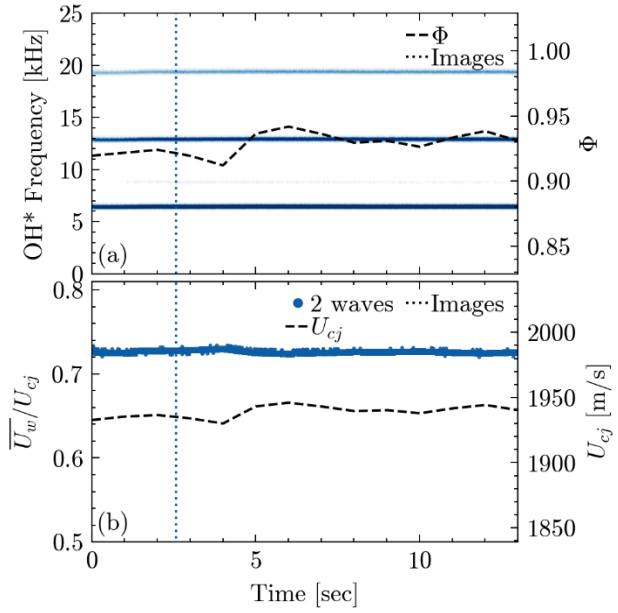

Fig. 13 OH* probe spectrogram for short timescale two-wave (S2) with equivalence ratio (a) and average wave speed normalized by CJ speed with the CJ speed (b).

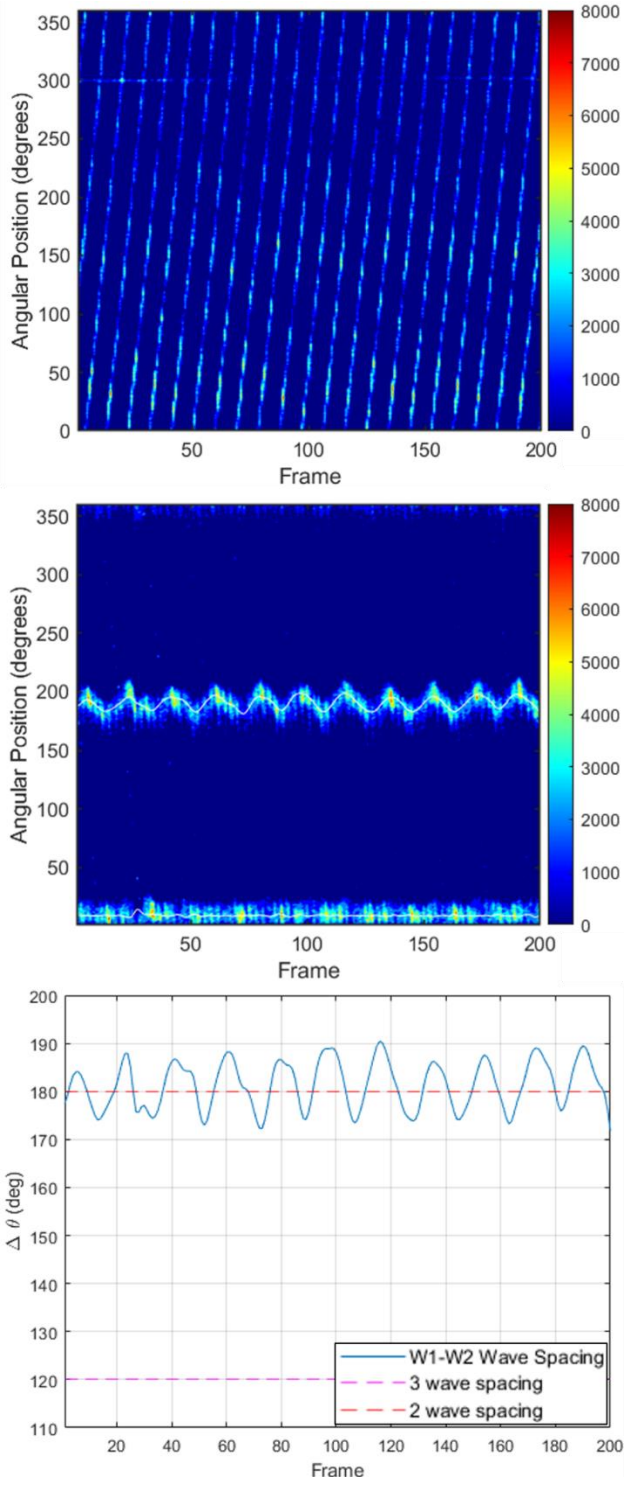

Fig. 14 Short timescale wave spacing for two-wave operation (S2).

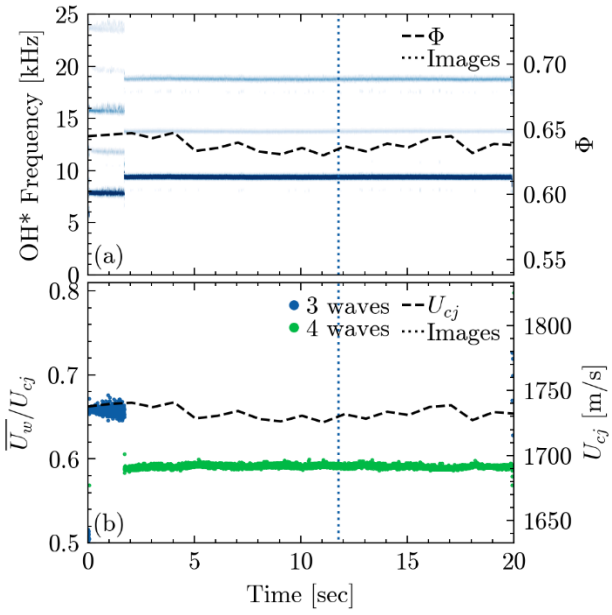

Fig. 15 OH* probe spectrogram for short timescale four-wave (S4) with equivalence ratio (a) and average wave speed normalized by CJ speed with the CJ speed (b).

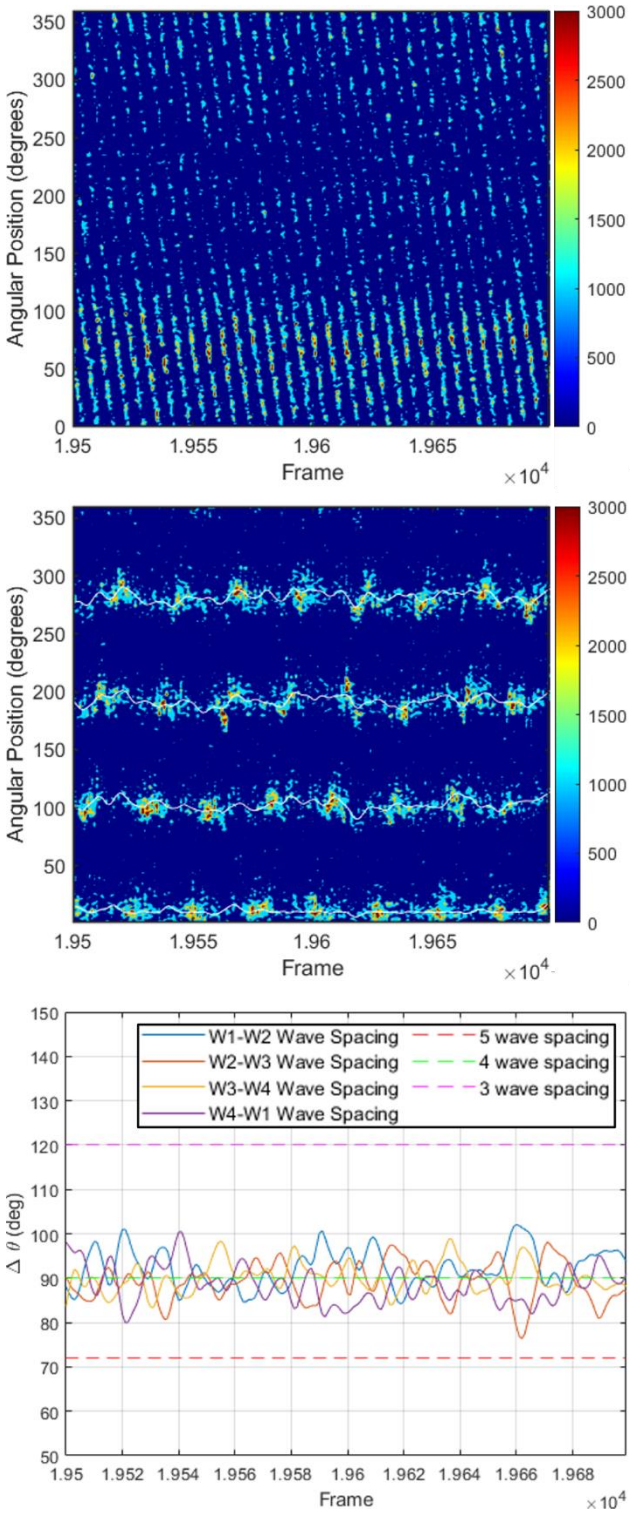

Fig. 16 Short timescale wave spacing for four-wave operation (S4).

Although variation of the wave separation is observed in Figure 16 to be ±10°, the behavior is not periodic and is not consistent with the LCO behavior observed in other cases, resulting in an absence of sidebands within the spectrogram shown in Figure 15. For this reason, case S4 is deemed non-LCO due to non-periodic variation of wave separation occurring in short timescales. Figures 14 and 16, representing LCO and non-LCO modes, show both periodic and non-periodic wave spacing present within modes that would otherwise be deemed equally spaced wave modes. This suggests that there does not need to be a specific event which causes wave spacing to become non-uniform to initiate LCO. Instead, certain process parameters may lead to dynamic states that promote existing non-uniform wave separations into a steady LCO mode.

D. Transitional LCO Wave Modes

Transition to and from LCO wave modes during sustained operation of the RDE constitute another observed modal behavior that is of particular interest. An example of this behavior is observed throughout the spectrogram of case T45 in Figure 17(a), where the mass flow rate of fuel is intentionally decreased resulting in a linear decrease in equivalence ratio from 1.0 to 0.48, also plotted in Figure 17(a). After the initial transient start-up, the spectrogram displays a four-wave LCO mode beginning at 2 seconds with a strong dominate carrier frequency flanked with sideband frequencies. However, as the run approaches 12.5 seconds the LCO mode starts to become less consistent, which is visible with changes in strength of the sideband frequencies. As the equivalence ratio continuously decreases, the wave speed decreases until the mode transitions to a steady five wave mode around 12.5 seconds at an equivalence ratio of 0.6, with a single dominate frequency and no sidebands. The mean wave speeds stay between 55% to 66% of the CJ speed, as seen in Figure 17(b).

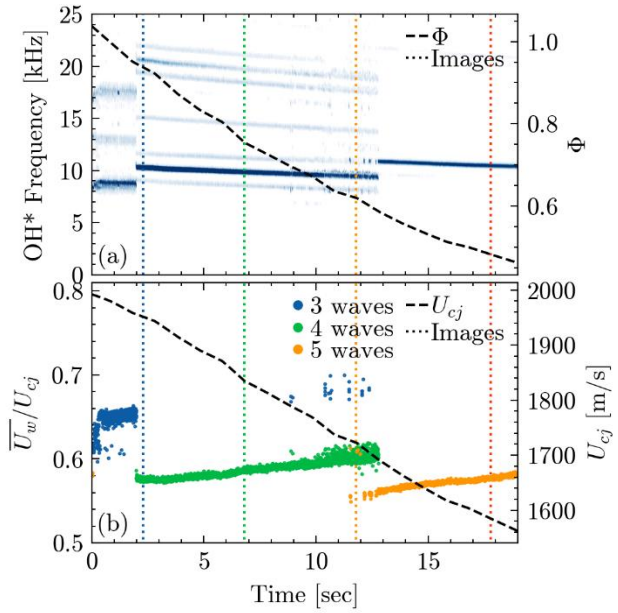

Fig. 17 OH* spectrogram for transitional four-wave LCO to five-wave mode (T45) with equivalence ratio (a); average wave speed normalized by CJ speed with CJ speed (b).

As previous done, images acquired at the times indicated by the vertical lines in Figure 17 are used to create the detonation surface, LCOV surface, and wave separation plots presented in Figure 18. The images confirm the four-wave LCO mode at 2.292, 6.792, and 11.792 seconds as well as the uniform five-wave mode at 17.792 seconds. Looking at the periodic wave spacing for the LCO mode, the deviation increases with lowering equivalence ratio, moving from ±10°, to ±15°, to almost ±20° in Figure 18 (right). In addition to the increasing amplitude of the wave spacing prior to the mode change, the strength of the LCO appears to decrease as observed by diminishing sidebands just prior to the mode change at approximately 12.5 seconds. Higher degrees of wave spacing oscillation over longer periods of time eventually lead to an ascending mode change. After the transition to five waves, the wave spacing returns to a more uniform spacing state, with small differences attributed to noise, inconsistent with LCO.

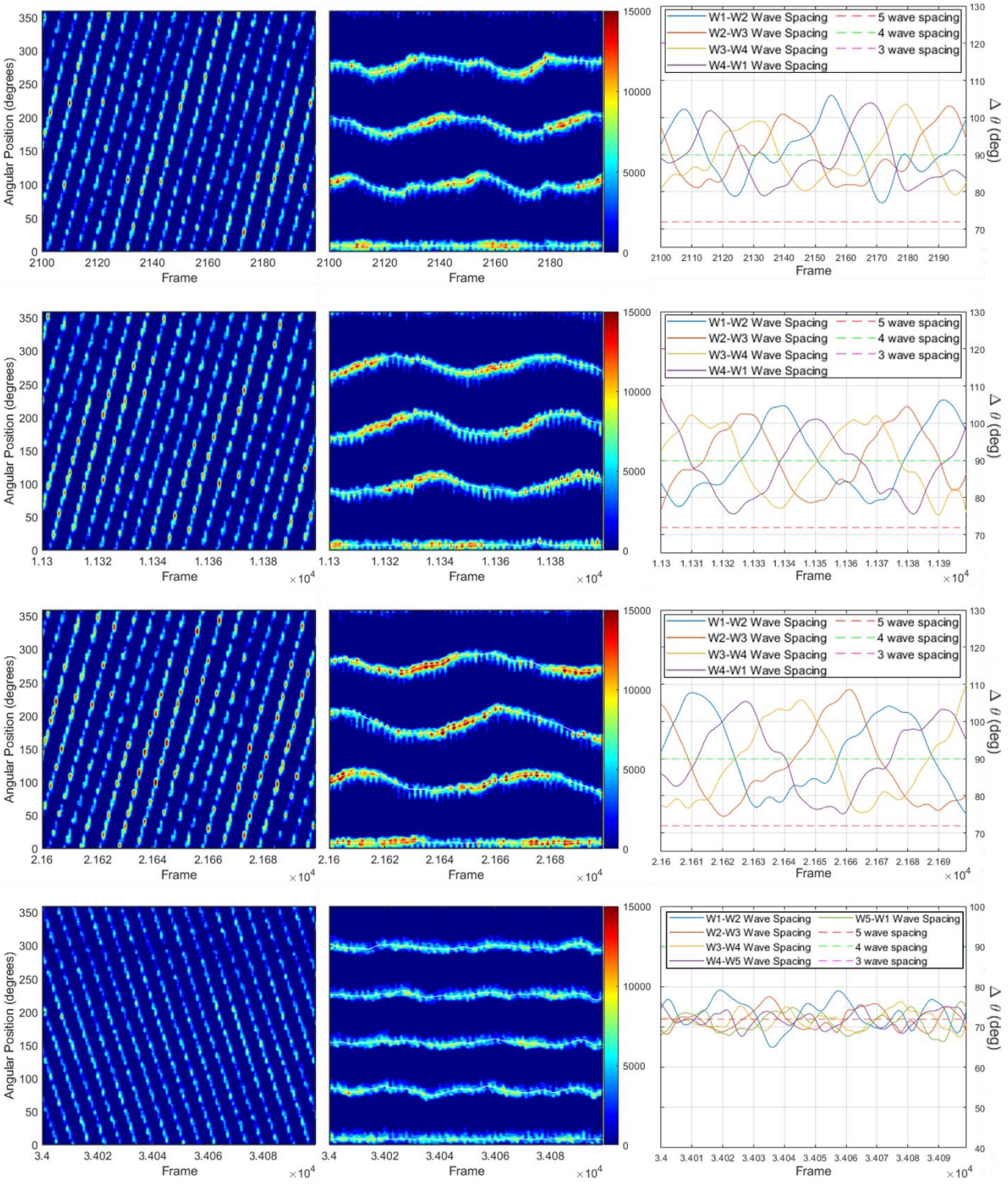

Fig. 18 T45 LCO detonation surface T45 (left), LCOV surface (center), and wave separation (right) for increasing equivalence ratio.

Opposite to case T45, case T54 results from an increasing equivalence ratio from 0.49 to 0.90. During this test run, the fuel flow rate is not continuously increased; instead, the fuel is changed with explicit step changes, which are

apparent in the spectrogram and equivalence ratio of Figure 19(a). After the initial transient start-up, a uniform five-wave mode persists until a transition at 8.5 seconds and an equivalence ratio of 0.62 to a four-wave LCO mode. After 15 seconds, the mode enters a transitional state, bouncing between four LCO waves, four uniformly spaced waves, and three uniformly spaced waves with changing direction. The introduction of the sporadic uniformly spaced three-wave mode is thought to be the result of instability introduced by step changes in equivalence ratio. The mean wave speed stays between 55% to 68% of the CJ speed, as shown in Figure 19(b). The transition points and ranges between the T45 and T54 are remarkably consistent.

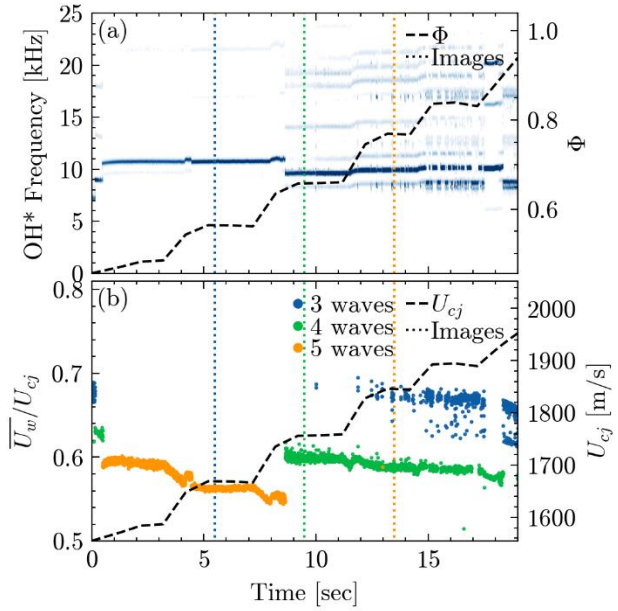

Fig. 19 OH* spectrogram for transitional five to four-wave LCO (T54) with equivalence ratio (a) average wave speed normalized by CJ speed with CJ speed (b).

Figure 20 shows detonation surfaces, LCOV surfaces, and wave separation trends for the three times indicated as vertical lines in Figure 19. High speed imaging confirms an early presence of five equally spaced waves at 5.482 seconds, followed by a transition to four LCO waves seen at 9.482 and 13.482 seconds. Wave spacing at the first sampling point appears to be random, meeting expectations based on the portion of the spectrogram with no sidebands. Across the two subsamples following the mode change, the spacing of four LCO waves demonstrates oscillations over shorter periods, leading to strengthened sidebands in the spectrogram.

While the exact cause of the LCO wave mode is not currently understood, it seems clear that these modes exist as persistent dynamic states of the system. Of particular interest throughout the current subsection is the appearance and sustainment of LCO modes across sweeping equivalence ratios. While steady state operation of the RDE is of vital

interest, the ability to operate across a variety of modes with sustained detonations throughout a ramped state is also of importance, for example to accommodate varying load changes as a result of intermittent renewable power sources [17]. Cases T45 and T54 display a brief indication of this capability, with a need to further investigate process sweeps as a future work.

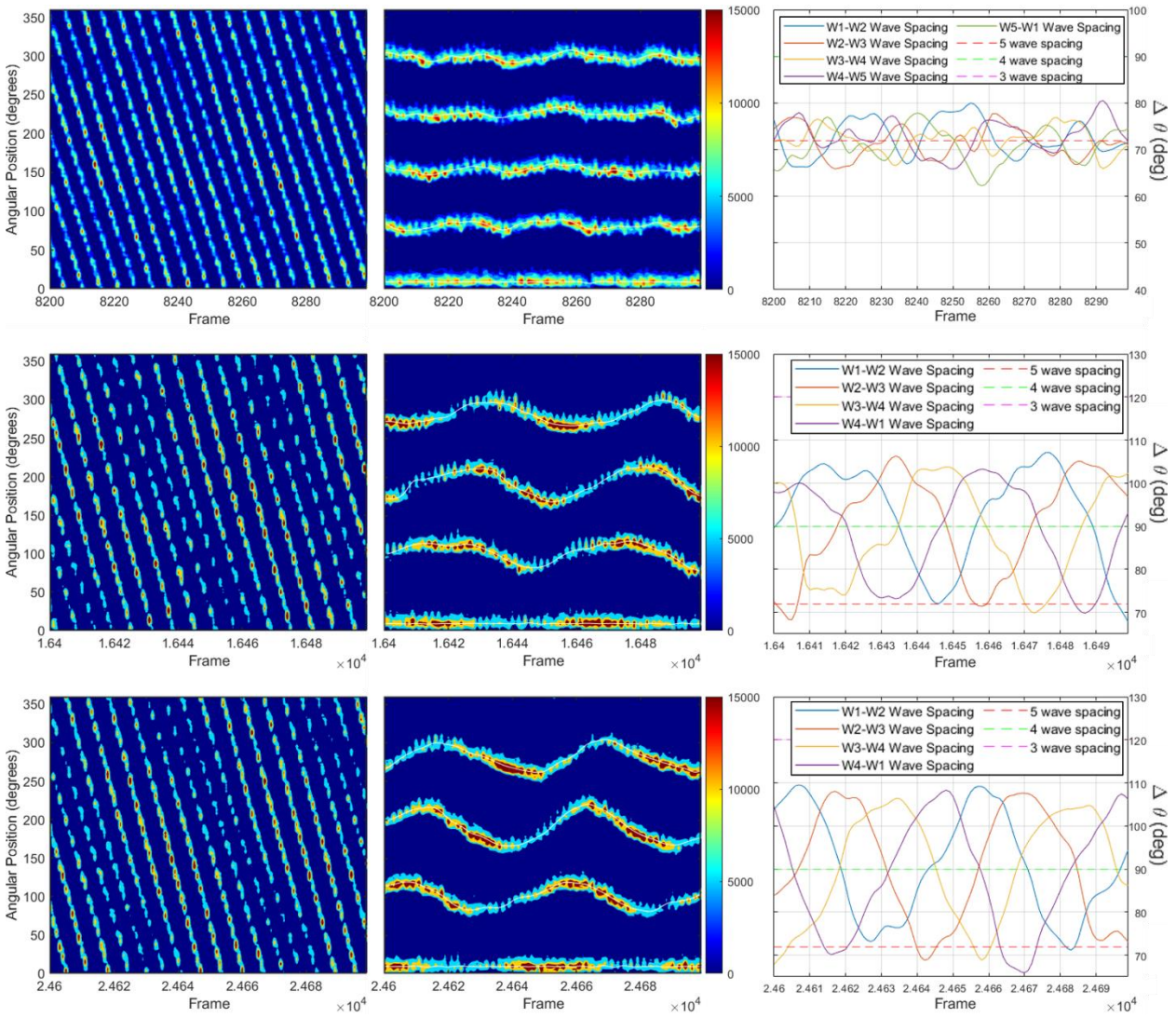

Fig. 20 Transitional LCO detonation surface T54 (left), LCOV surface (center), and wave separation (right) for decreasing equivalence ratio.

E. Discussion

Emission spectrums at the detonation plane dominated by OH* (hydrogen-air combustion) have been measured experimentally [18] and computed [19] across a range of operating conditions. Knowing this, high-speed chemiluminescence measurements applied to the research topic of experimental RDEs offers a distinct ability to

qualitatively analyze detonation wave behaviors and characteristics. Additionally, OH* chemiluminescence signal strength in images has been used throughout the RDE community to study acoustic/detonative modes [20], heat release distributions [21], injection backflow and recovery [22], and a host of additional detonation interactions [23–25].

While a direct conversion from pixel intensity or signal strength to a quantitative unit of heat release or combustion efficiency is not straight-forward without conducting extensive calibration imaging systems photon conversion efficiency, comparative pixel intensity offers an analogous relationship to wave strength. Throughout this subsection, contrast of integrated pixel intensities representing individual wave bodies is leveraged as a relative scale of detonation wave strength. Scales of this correlation are applied only within short windows of images, not exceeding 200 frames, approximately 3.33 msec. In general, if a wave exhibits lower maximum pixel intensity than its partner, it is said to be weaker than its counterpart. For down-axis imaging, this assumes optimal optical alignment in which light collection is uniform across each pixel of the camera CCD array and around the circumference of the RDE.

To consider the local LCO behavior as a possible function of fill height, interactive behaviors of neighboring waves is investigated. In the following discussion, each unique wave set is discussed as a leading and lagging wave for comparison of relative wave strength and local wave separations. For each case presented, waves are traveling counterclockwise, and the wave with higher numbered label increment is the leading wave according to the detonation surface transformation. Because the selection of W1 in the creation of the shifted detonation surfaces is independent of any apparent dominance or influence on the mode, all possible wave sets are considered equally. For example, a four-wave mode is examined as the interactions of wave sets W1-W2, W2-W3, W3-W4, and W4-W1, where W2 leads W1, W3 leads W4, and so on.

Recall that values of the shifted detonation surface reflect the trapezoidal integration of pixels contained in an azimuthal bin, each containing approximately 72 pixels. This limits the influence of an erroneous pixel on the location of maximum intensities fit by the smoothing splines. Extending the application of wave-fit splines, the integrated pixel intensity along each wave is easily extracted from the shifted detonation surface. If $S_W(n)$ is the smoothing spline summarizing the angular location of a given wave, W, as a function of frame, then the intensity of the same wave is found by indexing $\Psi(z, n)$ according to Equation 9.

$$\xi_W(n) = \Psi(S_W(n), n) \tag{9}$$

Wave intensity of neighboring wave pairs are utilized to evaluate the wave-to-wave pixel difference. When the time-dependent wave-to-wave pixel difference, reflective of relative wave strength difference, is plotted against

angular separation for a pair of waves in Figure 21, a limit cycle structure is obtained for cases S2, T45, and Q5. To most easily compare the limit cycle structure of cases S2, T45, and Q5, the wave-to-wave pixel differences plotted in Figure 21 are min-max normalized. This adjusts the data such that the minimum value, which is a negative value indicating a stronger W2, is transformed to 0 while the maximum difference, corresponding to a stronger W1, is transformed to 1. This visualization confirms the LCO nature of the wave spacing for each mode type discussed in the previous subsections and suggests a potentially coupled relationship between wave strength and resultant wave spacing for a pair of waves.

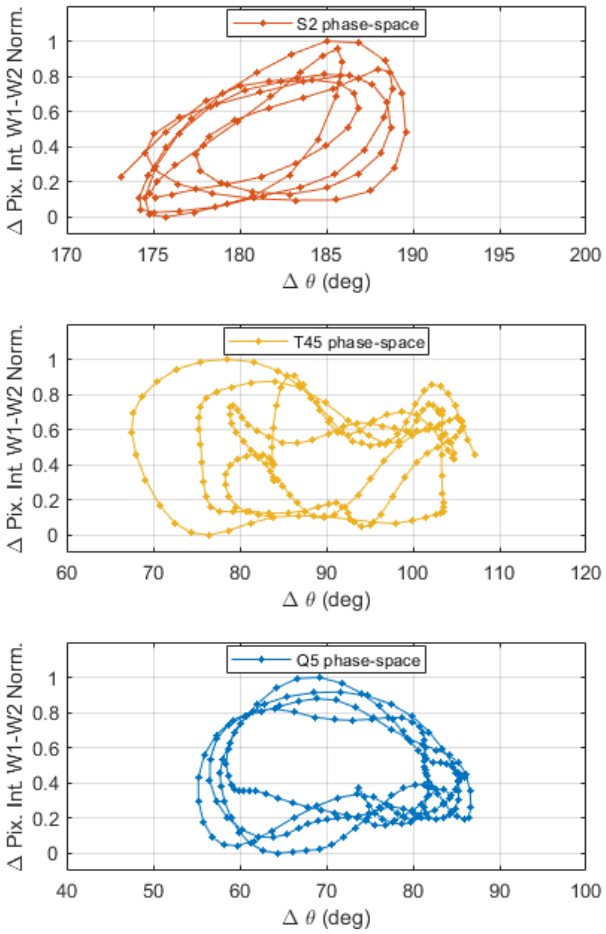

Fig. 21 Limit cycle structures visualized via normalized pixel intensity variation versus wave spacing for W1-W2 pairs among S2, T45, and Q5 cases.

The integrated pixel difference of a W_A-W_B wave set as a function of frames is computed as $\xi_{A-B}(n) = \xi_B(n) - \xi_A(n)$. In the subplots of Figures 22 and 23, pixel differences are plotted as blue dashed lines on the left y-axes for wave sets sampled from the S2, T45, and Q5 cases. These values are extracted directly from LCOV surfaces in Figures 14, 18, and 12, respectively. Among each case presented, a subplot corresponding to the relationships of each wave

pair is plotted. Interpreting this relationship for a given wave pair, positive values indicate a stronger leading wave, and negative values a stronger lagging wave. Further, positive slopes spanning from negative to positive values correspond to a trend of a weaker leading wave becoming increasingly stronger, to a point of equality at the $\xi_{A-B}(n) = 0$ threshold, subsequently surpassing the lagging wave in strength. The same occurrence favoring the lagging wave is demonstrated by negative slopes spanning from positive to negative values.

Assessing the possible interconnection of wave strength and LCOs, the differentiated angular separation is computed by Equation 10. In generic terms, Equation 10 utilizes the difference of wave angular positions provided by smoothing spines $S_A(n)$ and $S_B(n)$ to describe the local wave separation rate of change, $\Delta\beta_{A-B}(n)$. Wave separation rate of change, having units of °/frame, is plotted for unique wave pairs of cases S2, and T45 in Figure 22 and case Q5 in Figure 23 as a solid orange line on the right y-axes.

$$\Delta\beta_{A-B}(n) = \frac{d(S_B(n) - S_A(n))}{dn} \tag{10}$$

The local wave separation rate of change can be deciphered as the acceleration or deceleration of wave separation, not that of an individual wave with angular acceleration. Therefore, terms such as rate of change, acceleration, and deceleration should not be confused with any descriptors of wave speed. As the angular separation between two waves increases, the local wave separation rate of change is positive. Negative values correspond to decreasing wave separation. Within a period of wave separation acceleration and deceleration, maximum and minimum wave separations occur at $\Delta\beta_{A-B}(n) = 0$. A positively sloped line passing through $\Delta\beta_{A-B}(n) = 0$ indicates a minimum wave spacing, and a negatively sloped line passing through $\Delta\beta_{A-B}(n) = 0$ indicates a maximum wave spacing.

In each of the subplots of Figures 22 and 23, the reciprocity of wave strength dominance is exchanged from leading and lagging waves in a clearly periodic manor. This reveals that no single wave maintains dominance in observed strength compared to any adjacent waves. It is expected, that if this trend were not observed across each wave pair, a dominant wave would eventually lead to larger vulnerability and possibly the elimination of a weaker wave. It is also clear that for all oscillating wave types (short timescale, transitional, and quasi-steady), local wave separation rate of change is periodic as well. Furthermore, traces are common in shape and scale within the period for each wave set throughout a study case. This demonstrates that no particular pair of waves experiences uniform separation or fluctuations excessive in scale compared to other wave pairs sharing the annulus region. If either extreme existed for any wave pair, instability leading to a modal change is thought to be likely.

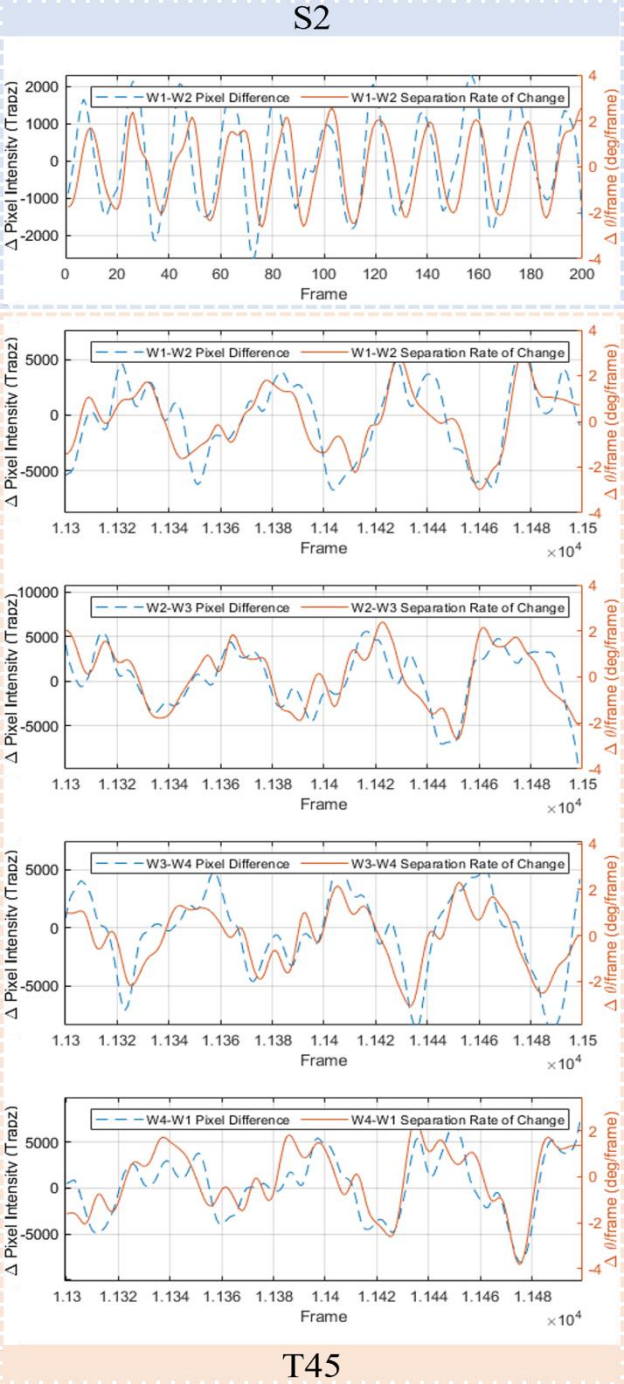

Fig. 22 Wave-to-wave pixel intensity difference (blue dashed line, left y-axis) and wave separation rate of change (orange line, right y-axis) for S2, and T45 cases.

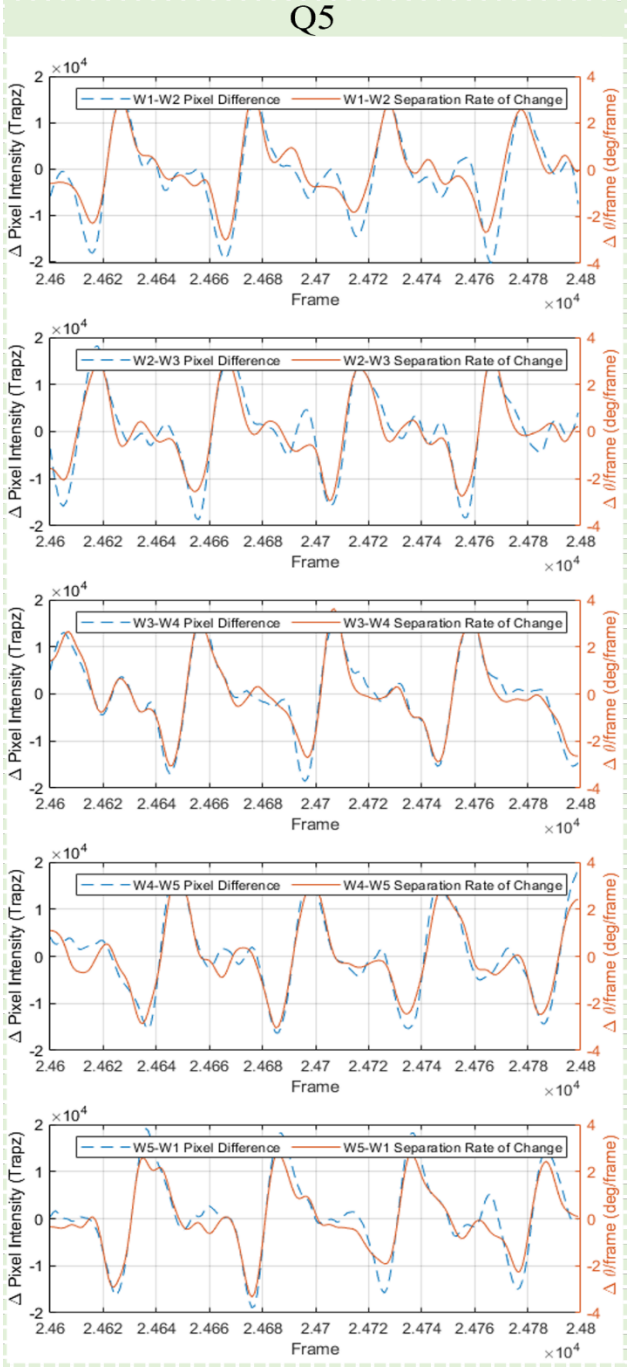

Fig. 23 Wave-to-wave pixel intensity difference (blue dashed line, left y-axis) and wave separation rate of change (orange line, right y-axis) for Q5 case.

Both functions plotted in Figures 22 and 23 offer uniquely valuable insights regarding LCO stability. Conclusions made possible by the comparison of the two functions are of even greater interest. Figures 22 and 23 overlay pixel difference associated with relative wave strength, and wave separation rate of change for individual wave sets. In this format, the two relationships appear to be deeply connected, illustrated by shared periods and signal shapes of the aligned curves. Combining understanding of each function suggests: shared positive values correspond to a stronger leading wave and increasing wave separation; shared negative values indicate a stronger lagging wave and decreasing wave separation; and shared zero values indicate equal wave strength, and maximum or minimum wave separation.

It appears that as the leading wave remains stronger than the lagging, their separation continually increases. As the strengthened leading wave travels further from the lagging wave, it simultaneously becomes closer to the next wave. Assuming a constant injector velocity, the strong wave begins to travel through shorter fill height, resulting in gradual weakening. Meanwhile, the lagging wave experiences a larger fill height due to the larger wave spacing and subsequently increased recovery time. This strengthens the lagging wave and decreases wave spacing until a critical point where both waves experience comparable fill heights, resulting in equal strength and a maximized wave spacing. As the two waves become closer, the fill heights increase and decrease for the leading and lagging waves, respectively, until the critical point of minimum spacing. Another possibility would be that of a periodic variation in the fuel and/or air injection velocity resulting from non-uniform injector recovery producing rich or lean pockets ahead of the detonation wave. Regardless of the source, this cycle repeats continuously throughout the experimental run time between each wave set. In contrast with global instabilities leading to mode changes described as *galloping* in other RDE literature, not adhering to the classical definition of galloping detonation, these persistent LCO behaviors do not appear to exhibit rapid acceleration or deceleration of wave spacing. Instead, the globally shared fluctuations show individual detonation waves potentially responding gradually to localized variation in fill height, resulting in persistent LCO modes.

VI. Conclusion

Limit cycle oscillation (LCO) wave modes are a particularly interesting observed state in RDEs induced by process conditions which lead to consistent oscillating wave spacing. Within the LCO wave mode, waves experience periodic acceleration and deceleration, thought to be a response to local fill height variations. What is most intriguing is the

graceful acceleration and deceleration of waves in response to upstream changes opposed to continuing at the same speed and catching up to the wave in front. It is precisely this attribute that allows for persistent LCO modes to be maintained seemingly indefinitely, as the boundary conditions of the detonation channel remain consistent. Unfortunately, it is still unknown if these LCO dynamic states have detrimental effects on the performance of an RDE either through reduction in pressure gain, changes in combustion efficiency, NOx formation or unsteadiness of exhaust flow. They are repeatable states that are strongly tied to the process parameters, and as such the wave modes are correlated to the process flow rates, back pressure, and inlet air temperature. Results presented warrant the consideration of LCO waves as a repeatable, persistent wave mode that may impact the targeted performance of the device in a turbine-integrated setting.

Acknowledgments

This work was performed in support of the U.S. Department of Energy's Fossil Energy and Carbon Management's Hydrogen with Carbon Management Technologies Program and executed through the National Energy Technology Laboratory (NETL) Research & Innovation Center's Turbines Program. This project was funded by the U.S. Department of Energy, National Energy Technology Laboratory, in part, through a site support contract. Neither the United States Government nor any agency thereof, nor any of their employees, nor the support contractor, nor any of their employees, makes any warranty, express or implied, or assumes any legal liability or responsibility for the accuracy, completeness, or usefulness of any information, apparatus, product, or process disclosed, or represents that its use would not infringe privately owned rights. Reference herein to any specific commercial product, process, or service by trade name, trademark, manufacturer, or otherwise does not necessarily constitute or imply its endorsement, recommendation, or favoring by the United States Government or any agency thereof. The views and opinions of authors expressed herein do not necessarily state or reflect those of the United States Government or any agency thereof.

References

[1] Sousa, J., Paniagua, G., and Collado Morata, E., "Thermodynamic Analysis of a Gas Turbine Engine with a Rotating Detonation Combustor," *Applied Energy*, Vol. 195, June 2017, pp. 247–256. https://doi.org/10.1016/j.apenergy.2017.03.045

[2] Ferguson, D. H., O'Meara, B., Roy, A., and Johnson, K., "Experimental Measurements of NOx Emissions in a Rotating Detonation Engine," *AIAA Scitech 2020 Forum*, AIAA 2020-0204, Orlando, FL, 2020. https://doi.org/10.2514/6.2020-0204

[3] Voitsekhovskii, B., "Stationary Spin Detonation," *Soviet Journal of Applied Mechanics and Technical Physics*, Vol. 3, 1960, pp. 157-164.

[4] Nicholls, J. A., Cullen, R. E., and Ragland, K. W., "Feasibility Studies of a Rotating Detonation Wave Rocket Motor," *Journal of Spacecraft and Rockets*, Vol. 3, No. 6, 1966, pp. 893–898. https://doi.org/10.2514/3.28557.

[5] Bennewitz, J. W., Bigler, B. R., Pilgram, J. J., and Hargus, W. A., "Modal Transitions in Rotating Detonation Rocket Engines," *International Journal of Energetic Materials and Chemical Propulsion*, Vol. 18, No. 2, 2019, pp. 91–109. https://doi.org/10.1615/IntJEnergeticMaterialsChemProp.2019027880

[6] Batista, A., Ross, M., Lietz, C., and Hargus, W., "Descending Modal Transition Dynamics in a Large Eddy Simulation of a Rotating Detonation Rocket Engine," *Energies*, Vol. 14, No. 12, 2021, pp. 3387. https://doi.org/10.3390/en14123387

[7] Koch, J., Kurosaka, M., Knowlen, C., and Kutz, J. N., "Multiscale Physics of Rotating Detonation Waves: Autosolitons and Modulational Instabilities," *Physical Review E*, Vol. 104, August 2021, pp. 024210. https://doi.org/10.1103/PhysRevE.104.024210

[8] Wolański, P., "Rotating Detonation Wave Stability," *23rd ICDERS*, ICDERS 2011-0211, Irvine, California, 2011.

[9] Brophy, C. M., and Codoni, J. R., "Experimental Performance Characterization of an RDE Using Equivalent Available Pressure," *AIAA Propulsion and Energy 2019 Forum*, AIAA 2019-4212, Indianapolis, IN, 2019. https://doi.org/10.2514/6.2019-4212

[10] Bennewitz, J. W., Bigler, B. R., Schumaker, S. A., and Hargus, W. A., "Automated Image Processing Method to Quantify Rotating Detonation Wave Behavior," *Review of Scientific Instruments*, Vol. 90, No. 6, 2019, pp. 1–12. https://doi.org/10.1063/1.5067256

[11] Journell, C.L., Gejji, R.M., Walters, I.V., Lemcherfi, A.I., Slabaugh, C.D., and Stout, J.B., "High-Speed Diagnostics in a Natural Gas–Air Rotating Detonation Engine," *Journal of Propulsion and Power*, Vol. 36, No. 4, 2020, pp. 498-507. https://doi.org/10.2514/1.B37740

[12] Boening, J. A., Heath, J. D., Byrd, T. J., Koch, J. V., Mattick, A. T., Breidenthal, R. E., Knowlen, C., and Kurosaka, M., "Design and Experiments of a Continuous Rotating Detonation Engine: a Spinning Wave Generator and Modulated Fuel/Oxidizer Mixing," *52nd AIAA/SAE/ASEE Joint Propulsion Conference*, AIAA 2016-4966, Salt Lake City, UT, 2016. https://doi.org/10.2514/6.2016-4966

[13] Koch, J., Mitsuru K., Carl K., and Kutz, J.N, "Multi-scale Physics of Rotating Detonation Engines: Autosolitons and Modulational Instabilities," *Physics Review* E, Vol. 104, August 2021, pp. 024210. https://doi.org/ 10.1103/PhysRevE.104.024210

[14] Anand, V., St. George, A., Driscoll, R., and Gutmark, E., "Characterization of Instabilities in a Rotating Detonation Combustor," *International Journal of Hydrogen Energy*, Vol. 40, No. 46, 2015, pp. 16649–16659. https://doi.org/10.1016/j.ijhydene.2015.09.046

[15] Bluemner, R., Bohon, M.D., Paschereit, C.O., and Gutmark E.J., "Counter-rotating Wave Mode Transition Dynamics in an RDC," *International Journal of Hydrogen Energy*, Vol. 44, No. 14, 2019, pp. 7628-7641. https://doi.org/10.1016/j.ijhydene.2019.01.262

[16] Rong, G., Cheng, M., Sheng, Z., Liu, X., Zhang, Y., and Wang, J., "The Behavior of The Propagating Velocity of Rotating Detonation Waves and Counter-Rotating Shock Waves in a Hollow Combustor," *Acta Astronautica*, Vol. 200, November 2022, pp. 371–387. https://doi.org/10.1016/j.actaastro.2022.08.033,

[17] Abudu, K., Igie, U., Roumeliotis, I., and Hamilton, R., "Impact of Gas Turbine Flexibility Improvements on Combined Cycle Gas Turbine Performance," *Applied Thermal Engineering*, Vol. 189, May 2021, pp. 116703. https://doi.org/https://doi.org/10.1016/j.applthermaleng.2021.116703

[18] Rankin, B. A., Richardson, D. R., Caswell, A. W., Naples, A. G., Hoke, J. L., and Schauer, F. R., "Chemiluminescence Imaging of an Optically Accessible Non-Premixed Rotating Detonation Engine," *Combustion and Flame*, Vol. 176, February 2017, pp. 12–22. https://doi.org/10.1016/j.combustflame.2016.09.020

[19] Feleo, A., France, J., White, L. W., and Gamba, M., "Evaluation of OH Emission for Determining Operation of a Rotating Detonation Engine," *AIAA Scitech 2019 Forum*, AIAA 2019-2252, San Diego, CA, 2019. https://doi.org/10.2514/6.2019-2252

[20] Johnson, K.B., Ferguson, D.H., Nix, A.C., and Tallman, Z., "Wave Detection and Tracking Within a Rotating Detonation Engine Through Object Detection," *Journal of Propulsion and Power*, Vol. 39, No. 4, 2023, pp. 612-625. https://doi.org/10.2514/1.B38960

[21] He, L., Guo, Q., Gong, Y., Wang, F., and Yu, G., "Investigation of OH* Chemiluminescence and Heat Release in Laminar Methane–Oxygen Co-Flow Diffusion Flames," *Combustion and Flame*, Vol. 201, March 2019, pp. 12-22. https://doi.org/10.1016/j.combustflame.2018.12.009

[22] Hsu, P. S., Slipchenko, M. N., Jiang, N., Fugger, C. A., Webb, A. M., Athmanathan, V., Meyer, T. R., and Roy, S., "Megahertz-Rate OH Planar Laser-Induced Fluorescence Imaging in a Rotating Detonation Combustor," *Optics Letters*, Vol. 45, No. 20, 2020, pp. 5776-5779. https://doi.org/10.1364/ol.403199

[23] Katta, V. R., Cho, K. Y., Hoke, J. L., Codoni, J. R., Schauer, F. R., and Roquemore, W. M., "Effect of Increasing Channel Width on the Structure of Rotating Detonation Wave," *Proceedings of the Combustion Institute*, Vol. 37, No. 3, 2018. https://doi.org/10.1016/J.PROCI.2018.05.072

[24] Rankin, B.A., Fotia, M.L., Naples, A.G., Stevens, C.A., Hoke, J.L., Kaemming, T.A., Theuerkauf, S.W., and Schauer, F.R.,

"Overview of Performance, Application, and Analysis of Rotating Detonation Engine Technologies," *Journal of Propulsion and Power*, Vol. 33, No. 1, 2017, pp. 131-143. https://doi.org/10.2514/1.B36303

[25] Tobias, J., Depperschmidt, D., Welch, C., Miller, R., Uddi, M., Agrawal, A. K., and Daniel, R., Jr., "OH* Chemiluminescence Imaging of the Combustion Products from a Methane-Fueled Rotating Detonation Engine," *Journal of Engineering for Gas Turbines and Power*, Vol. 141, No. 2, 2019, pp. 021021. https://doi.org/10.1115/1.4041143